Effects of dilute substitutional solutes on interstitial carbon in α-Fe: Interactions and associated carbon diffusion from first-principles calculations

Peitao Liu, Weiwei Xing, Xiyue Cheng, Dianzhong Li, Yiyi Li, and Xing-Qiu Chen*

Shenyang National Laboratory for Materials Science, Institute of Metal Research, Chinese Academy of Sciences, Shenyang 110016, China

(Received 1 December 2013; revised manuscript received 6 July 2014; published 28 July 2014)

By means of first-principles calculations coupled with the kinetic Monte Carlo simulations, we have systematically investigated the effects of dilute substitutional solutes on the behaviors of carbon in α-Fe. Our results uncover the following. (i) Without the Fe vacancy the interactions between most solutes and carbon are repulsive due to the strain relief, whereas Mn has a weak attractive interaction with its nearest-neighbor carbon due to the local ferromagnetic coupling effect. (ii) The presence of the Fe vacancy results in attractive interactions of all the solutes with carbon. In particular, the Mn-vacancy pair shows an exceptionally large binding energy of -0.81 eV with carbon. (iii) The alloying addition significantly impacts the atomic-scale concentration distributions and chemical potential of carbon in the Fe matrix. Among them, Mn and Cr increase the carbon chemical potential, whereas Al and Si reduce it. (iv) Within the dilute scale of the alloying solution, the solute concentration- and temperature-dependent carbon diffusivities demonstrate that Mn has a little impact on the carbon diffusion, whereas Cr (Al or Si) remarkably retards the carbon diffusion. Our results provide a certain implication for better understanding the experimental observations related with the carbon solubility limit, carbon microsegregation, and carbide precipitations in the ferritic steels.

DOI: 10.1103/PhysRevB.90.024103 PACS number(s): 66.30.Jt, 71.15.Nc, 71.15.Mb

I. INTRODUCTION

Carbon is one of the most common interstitial atoms in Fe-based alloys. Its addition can significantly improve the strength and hardness of steels by the solution strengthening and carbide precipitation strengthening [1]. Carbon is also incorporated into the surface layers by carburizing to enhance the mechanical properties of steels. Besides carbon, many other alloying elements (i.e., 3*d*, 4*d*, and 5*d* transition metals) are also added to improve the performance of the steels. Undoubtedly, the alloying elements would inevitably interact with carbon. Their addition would not only result in the lattice distortion and the local strain field due to the size factor of solutes, but also induce chemical or electronic effects on the soluble carbon atoms. They would trap or repel carbon, thereby affecting the behaviors of carbon in steels, such as the carbon solubility limit [2,3], microsegregation [4,5], diffusion [6–9], and carbide precipitations [10–12].

In comparison with other alloying elements in steels, carbon is lighter in mass, smaller in size, and lower in the electronic valence number. Therefore, it is highly difficult to experimentally identify carbon's behaviors in steels within the atomic scale. In particular, since in α-Fe the carbon solubility is very limited and its kinetics are very slow, it would require a long time to yield a true equilibrium. Although many studies have been performed to analyze the solute-carbon interactions, most understandings were derived from the sophisticated mechanical spectroscopic measurements. From the viewpoint of atomistic interactions, many questions remain open. For instance, through the internal friction measurements combined with the infrared analysis of carbon, Saitoh *et al.* [3] reported that in α-Fe Mn and Cr hardly altered the carbon solubility limit, whereas P and Si enhance it. The reasons for these behaviors still remain unclear. It is also well known that the carbon microsegregation is more serious in high-Mn steels, as observed by both Suzuki *et al.* [4] and Lu *et al.* [5]. However, the in-depth mechanism has not been resolved. Therefore, it would be highly desirable to elucidate the atomistic interactions between solutes and carbon in α-Fe, which could provide better understanding for the phase equilibria, phase diagrams and mechanical as well as physical properties [13].

To date, *ab initio* calculation based on the density functional theory (DFT) has been demonstrated to be a powerful tool to accurately evaluate the atomic interactions and understand the basic atomic phenomena involved. For instance, Jiang and Carter [14,15] investigated the carbon dissolution and diffusion in the ferrite and austenite, as well as the carbon adsorption and diffusion into Fe (110) and Fe (100) surfaces from first-principles calculations. Domain *et al.* [16] discussed the interactions of one C atom with an Fe vacancy, another C atom, and the self-interstitial atoms in α-Fe. They concluded that an Fe vacancy could bind two carbon atoms at most and the carbon-carbon interactions were revealed to be mostly repulsive. Afterwards, the interactions of an Fe vacancy with multiple C atoms in α-Fe were investigated in detail by Ohnuma *et al.* [17], who claimed that an Fe vacancy would bind four carbon atoms at most, but the system with a vacancy binding three C atoms was the most energetically stable. Yan *et al.* [18] even studied the interactions of C-N and C-N vacancy in α-Fe. They found that both C and N atoms would separate away from each other as far as possible in steels. Furthermore, utilizing the derived *ab initio* binding energies, Becquart *et al.* [19] constructed the so-called Fe-C potential within the framework of embedded atom method (EAM), determining the interaction of the carbon atoms with a screw dislocation. By combining first-principles calculations with the kinetic Monte Carlo (kMC) method, the Si impacts on the carbon diffusivity in α-Fe have been investigated by Simonovic *et al.* [20]. Very recently, Bakaev *et al.* [21] explored the interactions of some minor alloying elements in ferritic steels with interstitial carbon atom using *ab initio* calculations. They

*Corresponding author: xingqiu.chen@imr.ac.cn

found that Mn exhibits peculiar behavior. Contrary to other elements, Mn shows attractive interactions with carbon in the first- and second-nearest-neighbor sites [21].

Although some interactions [i.e., vacancy-carbon (or transition-metal solutes), carbon-carbon (or nitrogen), and solute-solute ones] have already been investigated, theoretically, the systematic studies on the interactions between substitutional solutes and carbon in α-Fe are rare, not to mention a unified understanding. The work we present here is intended to contribute to such an understanding from the perspective of state-of-the-art *ab initio* calculations by systematically elucidating the solute-C interactions, solute-vacancy-C interactions, and the impacts of the substitutional solutes on the carbon's distribution, chemical potential, and diffusion. These results would be definitely useful for the in-depth understanding of the carbon solubility limit, carbide precipitations, and the occurrence of carbon microsegregation.

II. METHODOLOGY

A. First-principles calculations and binding energies

Our calculations were based on the framework of DFT [22,23] as implemented in the Vienna *Ab initio* Simulation Package (VASP) [24,25]. All calculations were performed using the projector augmented wave (PAW) [26] potentials and the generalized-gradient approximation (GGA) within the Perdew-Burke-Ernzerhof (PBE) [27] exchange-correlation function, which has been proved to provide an accurate description of the magnetic and energetic properties of Fe bulk phases [28]. We used a Fermi smearing of electronic occupancy with a width of 0.05 eV, and a plane-wave cutoff energy of 500 eV, which has been found to be sufficient for precise energetics for all the elements considered in present work. Spin-polarized calculations were performed by considering the ferromagnetic ordering of Fe. The ion relaxations were performed at constant volume rather than at constant pressure, since the former one was found more suitable for the bcc-type cells in the impurities calculations [29]. The quasi-Newton algorithm was used to capture the minimum energy. The local magnetic moments and local density of states were calculated through the evaluation of the spin density within the Wigner-Seitz spheres around nuclei, the values of which adopted here were the recommended ones for the VASP code.

All the binding-energy calculations were based on a $3 \times 3 \times 3$ bcc unit cell, which contains 54 Fe atoms in the defect-free state. A $5 \times 5 \times 5$ $\vec{k}$-mesh grid generated by the Monkhorst-Pack scheme was used to sample the Brillouin zone, which has been revealed to be large enough to calculate the formation and binding energies for carbon with point defects [14,15]. Certainly, we have doubly checked the supercell convergence by computing the carbon solution enthalpy and the Fe vacancy formation energy using a larger $4 \times 4 \times 4$ supercell with $3 \times 3 \times 3$ $\vec{k}$-mesh grid. It is found that the energy differences between these two supercells are both less than 0.01 eV. To aid the computational efficiency, the projections operators were evaluated in real space because of the larger number of atoms in a supercell [30]. In agreement with the published results [14,15], carbon was found to occupy the most stable octahedral interstitial site (*o* site). Our calculations also revealed that the transition-metal elements, Al and Si, would substitute Fe site due to their comparatively large atomic size. For the α-Fe, the calculated lattice parameter and magnetic movement are 2.83 Å and 2.2 μ_B/atom, respectively, in good agreement with the experimental data of 2.86 Å and 2.2 μ_B/atom [31].

The binding energies are used to evaluate the interactions. In cases where the defect cluster contains two point defects, the binding energies are defined as

$$E_b^{i,j} = \frac{1}{m}[E_{D-(i+j)} - E_{D-i} - E_{D-j} + E_{\text{ref}}], \qquad (1)$$

where E_{D-i} and E_{D-j} are the total energy of the supercell with the point defects i and j, respectively, $E_{D-(i+j)}$ the energy of the supercell containing both point defects i and j, and E_{ref} the energy of the defect-free supercell, which is used to balance the number of the Fe atoms. m is the multiplicity considering the finite size and the periodicity of the cell [20]. For instance, if the substitutional atom is placed at [000] site and carbon is at [3/2 00] site, the substitutional atom would interact with carbon twice, and thus m equals to 2.

If the defect cluster contains three point defects, two different binding energies: The total binding energy and the incremental binding energy would be defined [30]. The total binding energy [30], representing the stability of the system with respect to the isolated defect, is defined as the energy difference between the supercell with the triple defects and the three supercells with individual point defects,

$$E_b^{i,j,k} = E_{\text{Triple}-(i+j+k)} - E_{D-i} - E_{D-j} - E_{D-k} + 2E_{\text{ref}}, \qquad (2)$$

where $E_{\text{Triple}-(i+j+k)}$ is the energy of the supercell containing all three point defects. The incremental binding energy [30] is defined as the energy difference between the supercell with the triple defects and the supercells with a single point defect and a defect pair,

$$E_b^{i,j+k} = E_{\text{Triple}-(i+j+k)} - E_{D-i} - E_{\text{Pair}-(j+k)} + E_{\text{ref}}, \qquad (3)$$

where $E_{\text{Pair}-(j+k)}$ is the energy of the supercell containing a pair of defects. It should be noted that since the considered interaction distance within the defect cluster is short, the multiplicity m mentioned in Eq. (1) is 1 in Eqs. (2) and (3). According to the definition in Eqs. (1)–(3), a negative binding energy indicates a favorable and attractive interaction between defects, while a positive binding energy refers to an unfavorable and repulsive interaction. This convention will be used to explore and explain all the interactions in various configurations discussed below.

B. Computations of the influences of dilute solutes on carbon's distribution and chemical potential

At the dilute concentration, the substitutional solutes would randomly distribute in the α-Fe matrix where the individual solute atoms are far apart from each other. The carbon atoms, which diffuse much faster than the substitutional solutes, will arrange themselves around the solutes [20]. In the limit of low solute and carbon concentration and under the condition of thermodynamical equilibrium, the carbon-carbon (C-C) and

solute-solute (M-M) interactions can thus be neglected. In terms of the model proposed by Simonovic *et al.* [20], the probability f_{Rs} that a carbon atom is present at a certain distance Rs from solute M can be expressed as

$$f_{Rs} = f_\infty \exp\left[\frac{-E_b^{M,C}(Rs)}{k_B T}\right], \tag{4}$$

where $E_b^{M,C}(Rs)$ is the solute-C binding energy at the distance Rs. k_B and T represent the Boltzmann constant and the absolute temperature, respectively. As the distance approaches $Rs_{\max}$, where the solute-C interactions vanish, the fraction of octahedral sites filled with carbon atoms can be assumed to be a constant value of f_∞. The carbon concentration C_C with respect to the bcc lattice is then given as [20],

$$C_C = C_M \sum_{s=1}^{\max} n_s f_{Rs} + \left(3 - C_M \sum_{s=1}^{\max} n_s\right) f_\infty, \tag{5}$$

where the first sum concerns all the carbon atoms within the interaction range $s_{\max}$ of the solute atom, and the value "3" in the second term denotes three octahedral positions per atom in the bcc lattice. C_M is the concentration of the solute M on the bcc lattice sites, and n_s is the number of the octahedral sites on shell s of the solute. Practically, the carbon concentration C_C is fixed. Combining Eqs. (4) and (5), the carbon fraction beyond the interaction range [20] can be derived as follows:

$$f_\infty = \frac{C_C}{C_M \sum_{s=1}^{\max} n_s \exp\left[\frac{-E_b^{M,C}(Rs)}{k_B T}\right] + \left(3 - C_M \sum_{s=1}^{\max} n_s\right)}. \tag{6}$$

According to the theory of the ideal solution, the chemical potential of carbon far away from the solute atom can be approximated as [20]

$$\mu_C = \frac{dF}{dC_C} = \frac{dF}{df_\infty}\frac{df_\infty}{dC_C} \approx \mu_C^0 + 3k_B T \ln\left(\frac{f_\infty}{1 - f_\infty}\right)\frac{1}{3} = \mu_C^0 + k_B T \ln(f_\infty), \tag{7}$$

where F is the free energy and μ_C^0 is the reference chemical potential. It can be inferred from Eq. (7) that the chemical potential of carbon μ_C will reduce when f_∞ decreases.

C. Computations of kMC simulations

To evaluate the migration energy barrier of carbon in α-Fe in the presence of vacancy, solute M, or solute-vacancy pair, the climbing-image nudged elastic band (CI-NEB) [32,33] method was employed. This method provides a way to find a minimum energy pathway (MEP) given the initial and final states of a process. During the NEB calculations, the images were kept separated using a spring force constant of 5 eV/Å and then relaxed using a conjugate gradient algorithm until the maximum force acting on each atom was less than 0.01 eV/Å. Note that in the cases where the carbon migrates in the presence of the solutes, we have computed the migration energy barriers of the carbon for all the possible diffusion pathways (see Table III), as the direction in which carbon will choose to jump depends significantly on its surrounding environment. These barriers can be further used as inputs for the following kMC simulations.

Carbon diffusivity in the presence of the dilute solutes has been further derived by the kMC method, which can be used to simulate the dynamic properties within a larger time scale because the time step is updated during the simulations [34]. In the kMC simulations, we have employed a very large simulated box (a $30 \times 30 \times 30$ bcc unit cell with the periodical boundary condition). The bcc lattice positions were all occupied either by Fe or solute M atoms. The solutes were randomly distributed according to their atomic concentration. The solute-solute distance was kept far beyond their interactions to form an approximate dilute environment. It needs to be emphasized that the diffusions of solutes and Fe are neglected here as their diffusions are extremely lower than that of carbon in α-Fe [20]. For a carbon atom in pure α-Fe, the diffusion prefactor D_0 and the corresponding diffusion migration energy ΔE were measured to be $D_0 = 6.61 \times 10^{-7}$ m^2/s and $\Delta E = 0.83$ eV, respectively [35]. However, the experimental self-diffusion data of Fe were $D_0 = 6.8$–27.7×10^{-4} m^2/s and $\Delta E = 2.95$–3.10 eV [36]. Even at 1000 K, the carbon diffusivity is three orders of magnitude greater than the self-diffusivity of Fe. This fact is also similar for most other substitutional solutes [37]. Within this context, it is safe to assume that the dilute substitutional solutes and Fe atoms do not diffuse as compared to the carbon atoms.

Technically, only one single carbon atom is considered in our kMC simulations. It is randomly located at the octahedral site at the initial status and then is allowed to jump to the neighboring o sites according to the probability rates which are computed within the framework of the transition state theory (TST) [38]. The energy barrier of each jump is calculated through CI-NEB method [32,33]. The transition time between two consecutive jumps is determined by the probability rates. The detailed steps of our kMC simulations are further compiled as follows [34].

(i) For each jump of the carbon atom, the probability rate γ_i is calculated by $\gamma_i = \nu_0 \exp(\frac{-E_b^i}{k_B T})$ ($i = 1,2,3,4$), where E_b^i is the energy barrier for the jump direction i and ν_0 is the jump attempt frequency, which was calculated to be $\nu_0 = 6.476 \times 10^{13}$ s^{-1} based on the Einstein approximation [20]. Note that the maximum number of i is 4 for each jump because only four jump directions can be chosen from the current o site to the nearest-neighboring o site in the bcc lattice.

(ii) The total probability rate $F = \sum_{i=1}^{4} \gamma_i$ and the relative probability of each event $F_i = \sum_{j=1}^{i} \gamma_j / F$ are computed.

(iii) The jump event i is selected by obeying $\sum_{k=1}^{i-1} F_k < \mu \leqslant \sum_{k=1}^{i} F_k$, where μ is a uniform random number $\mu \in [0, 1]$.

(iv) Meanwhile, the time elapsed for the current time step is calculated by $\triangle t = -\ln(\xi)/F$ based on the residence-time algorithm [39], where ξ is another random number distributed uniformly in [0,1]. Then the physical time increases $t = t + \triangle t$.

The steps (i) to (iv) are repeated until the physical time reaches the specified time (about 20 000 jump steps) after the carbon atom has moved a certain distance R away from the original position. Finally, the carbon diffusivity D can be

derived from the Einstein relation [40],

$$\langle R^2 \rangle = 6Dt, \tag{8}$$

where $\langle R^2 \rangle$ denotes the mean square displacement of carbon obtained by averaging over long time and repeated simulations. The prefactor D_0 and the migration energy ΔE for the carbon diffusion can then be extracted by the empirical Arrhenius form of the diffusion equation [40],

$$D = D_0 \exp\left(\frac{-\Delta E}{k_B T}\right). \tag{9}$$

III. RESULTS AND DISCUSSIONS

A. Solute-carbon (M-C) interactions

In order to calculate the solute-C binding energies, we have constructed a model (Fig. 1) where the solute M substitutes an Fe atom and the carbon is inserted in different neighboring o sites with respect to the solute M. Figure 2 shows the binding energies between all the transition-metal elements from the groups 4 to 11 on the periodic table and the carbon at the 1nn (first-nearest-neighbor) to the 4nn (fourth-nearest-neighbor) site. It can be seen that the solute-C interactions for all the 4d and 5d row elements almost exhibit a similar tendency: The 1nn site is the least stable one at which carbon can stay due to the largest repulsive interactions. As the distance increases, the repulsive interactions decrease sharply. Carbon seems to prefer to stay at the 3nn site since this position is energetically lowest. However, their solute-C (at 3nn) binding energies are still positive except for Zr, Hf, and Ag, which have a very weak attractive interaction with carbon. With increasing the distance to the 4nn site, the binding energies become positive again.

The repulsion between all the 4d and 5d transition-metal elements and carbon is no surprise. Since these elements are larger in size than Fe, their insertions would definitely result in a large local strain. The weak attraction for Zr, Hf, and Ag binding with C at the 3nn site can also be explained by the elastic effects because the 3nn octahedral interstices impacted by these elements are less flattened than those in the pure α-Fe crystal structure. Interestingly, it has been found that those 4d or 5d solute-C binding energies on the 1nn shell can be nearly linearly correlated with the size factor (as defined in Ref. [41]) of those solutes, as illustrated in Fig. 3. With the increasing solute size factor, the repulsive interaction becomes more obvious. Hence, it can be inferred that the individual 4d

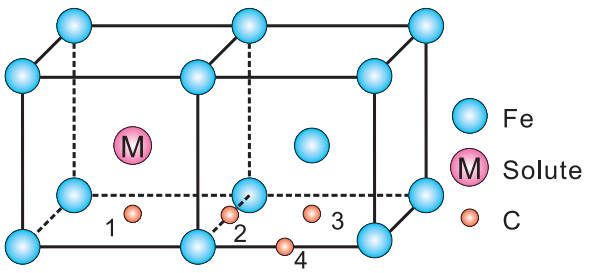

FIG. 1. (Color online) Solute M-C configurations. The C atom's site labeled i represents the first- to the fourth-nearest-neighbor (1nn to 4nn) octahedral site relative to the solute M in the bcc lattice.

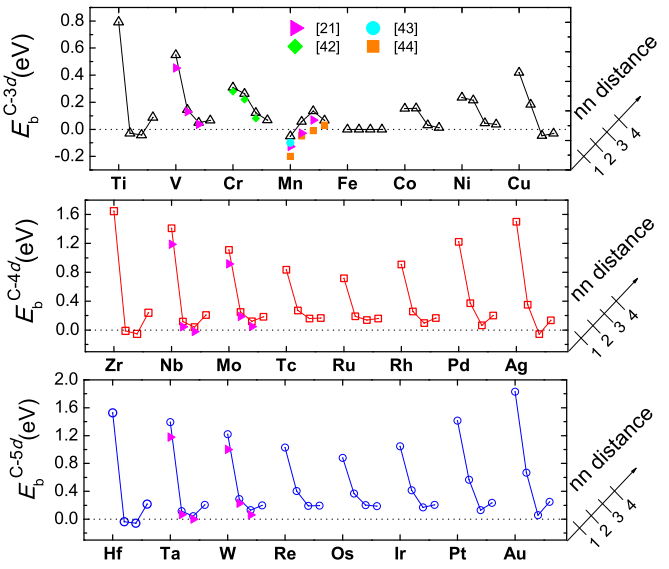

FIG. 2. (Color online) Solute M-C binding energies for the 3d (top panel), 4d (middle panel), and 5d (bottom panel) elements with C in the 1nn to 4nn octahedral site relative to the solute M.

and 5d row elements interact with the carbon atom mainly through the strain relief.

However, the binding energies for the 3d row elements exhibit a much more complicated behavior (see Fig. 2), because their M-C interactions depend not only on the solute size factors but also on the stronger magnetic couplings around Fe. Ti and V experience the antiferromagnetic coupling with their 1nn Fe atoms, whereas Cu has a weak ferromagnetic coupling with the 1nn Fe atoms (Table I). However, it needs to be emphasized that, although the magnetic coupling exists for them, their solute-C interactions are mainly dominated by the strain relief because of their relatively large solute size factors (Fig. 3). Therefore, these elements show behavior similar to

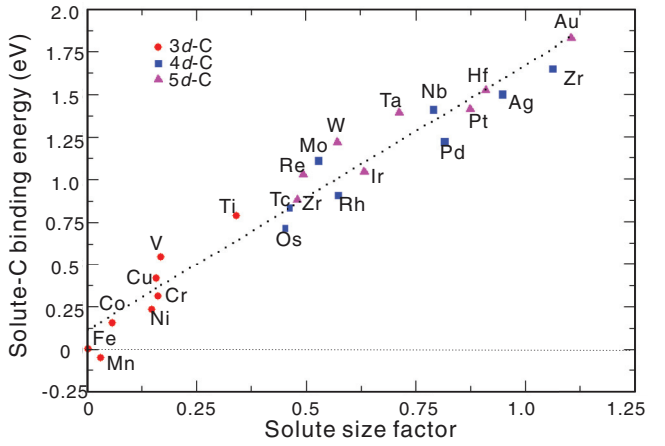

FIG. 3. (Color online) Solute M-C binding energies for the 1nn configuration as a function of the solute size factor. (The size factor of solute M in the Fe matrix is defined as $\Omega_{sf}^M = \frac{\Omega_M - \Omega_{Fe}}{\Omega_{Fe}}$, where Ω_M and Ω_{Fe} are the volume of supercell with the solute M and defect-free supercell, respectively. See more details in Ref. [41].)

TABLE I. Local magnetic moments (μ_B/atom) for the 1*nn* configuration of $Fe_{53}M_1C_1$ and for the cfg^5 of $Fe_{52}M_1C_1$ ($M = 3d$ transitional metal elements). The *inn* represents the *i*th-nearest-neighbor site of Fe relative to C.

M-C	*M*	C	Fe1*nn*	Fe2*nn*	Fe3*nn*	*M*-Vac-C	*M*	C	Fe1*nn*	Fe2*nn*	Fe3*nn*
Ti	−0.52	−0.09	1.46	2.10	2.38	Ti	−0.74	−0.13	2.15	2.51	2.52
V	−0.71	−0.08	1.53	2.14	2.39	V	−1.34	−0.15	1.71	2.03	2.04
Cr	−0.66	−0.07	1.56	2.15	2.39	Cr	−2.11	−0.12	0.93	2.09	2.11
Mn	0.68	−0.11	1.68	2.21	2.39	Mn	−2.67	−0.15	1.72	2.02	2.03
Fe	1.67	−0.14	1.67	2.20	2.38	Fe	2.42	−0.15	1.70	2.03	2.02
Co	1.22	−0.13	1.67	2.21	2.38	Co	1.70	−0.15	1.73	2.03	2.03
Ni	0.57	−0.12	1.60	2.17	2.36	Ni	0.92	−0.15	1.73	2.02	2.03
Cu	0.08	−0.12	1.47	2.10	2.35	Cu	0.18	−0.15	1.73	2.03	2.03

that of the the 4*d* or 5*d* elements of comparable sizes. In contrast, for the intermediate 3*d* elements the solute-C interactions are largely affected by the magnetic coupling effects. For instance, the metal Cr displays a repulsive interaction with C for all four configurations, consistent well with the theoretical data published by Sandberg *et al.* [42] (see Fig. 2). A similar situation has been observed for Co and Ni. The most striking case is Mn, which is the only element that shows an unusual character of the binding interaction with C. The 1*nn* Mn-C interaction is weakly attractive (Fig. 2) and is accompanied with the appearance of a ferromagnetic coupling with its 1*nn* Fe atoms.

The attractive Mn-C interactions were not only studied theoretically in Refs. [21,43,44], but also derived from experiments [45–48]. Numakura *et al.* [44] derived the Mn-C interaction energies using the molecular statics technique based on the empirical pairwise potentials. Similarly, they also reported the attractive Mn-C interaction on the 1*nn* shell but with a somewhat larger binding energy. This discrepancy might be attributed to their less accurate empirical pairwise potentials and their bad choice for the energy reference. In their calculations [44], they used the 5*nn* Mn-C interaction configuration as the reference energy because they believed that beyond the 5*nn* shell the Mn and carbon atoms should not interact with each other. However, according to our calculations, the Mn-C interaction energy at the 5*nn* configuration is not negligible (see Fig. 10). Medvedeva *et al.* [43] performed similar first-principles calculations and they also obtained an attractive Mn-C binding energy (−0.10 eV) for the 1*nn* configuration, which is quite accordant with our result (−0.08 eV). Besides, our results also agree well with the calculated data recently reported by Bakaev *et al.* [21] (see Fig. 2). Although all the calculated Mn-C binding energies are much lower than the experimentally estimated values (0.14–0.46 eV) [45–48], the theoretical results could better match the experimental ones if the actual Mn concentration and the formation of Mn_xC clusters were taken into account [43].

In order to elucidate the attractive Mn-C interaction on the 1*nn* shell, we analyzed the electronic structures including the charge density differences and local density of states compared with the opposite Ti-C binding case. As shown in Fig. 4(a), in the low-energy region from −7 to −5 eV of the density of states, a strong hybridization can be visualized between Mn and C 2*p*-like states, whereas in the Ti-C case the hybridization between Ti and C 2*p*-like states is relatively much weaker [Fig. 4(b)]. This fact can be further supported by their electronic density deformation maps which give a direct real-space visualization of local electronic rearrangements. It can be seen from Fig. 4(c) that the charge accumulation clearly occurs along the bond between Mn and C in the 1*nn* configuration, whereas less charges are accumulated between Ti and C [Fig. 4(d)]. In contrast, more charges accumulate between Ti and its 1*nn* Fe atoms in the Ti-C case. These results suggest that Mn atom binds strongly with the C atom rather than the Fe matrix, whereas the Ti atom shows contrary behavior.

In agreement with the analysis of electronic structures, it has been found that the magnetic couplings indeed significantly affect the Mn-C interactions. On the one hand, the magnetic interactions decrease the Mn-C binding energy from a positive non-spin-polarized value of 0.13 eV to a negative spin-polarized value of −0.08 eV, whereas they almost do not impact the Ti-C binding energy (spin-polarized, 0.79 eV, and non-spin-polarized, 0.77 eV). On the other hand, we found that the magnetic moment of Mn atom changes greatly from an antiferromagnetic spin moment of $-0.39\mu_B$ in $Fe_{53}Mn$ supercell to a ferromagnetic spin moment of $0.72\mu_B$ in

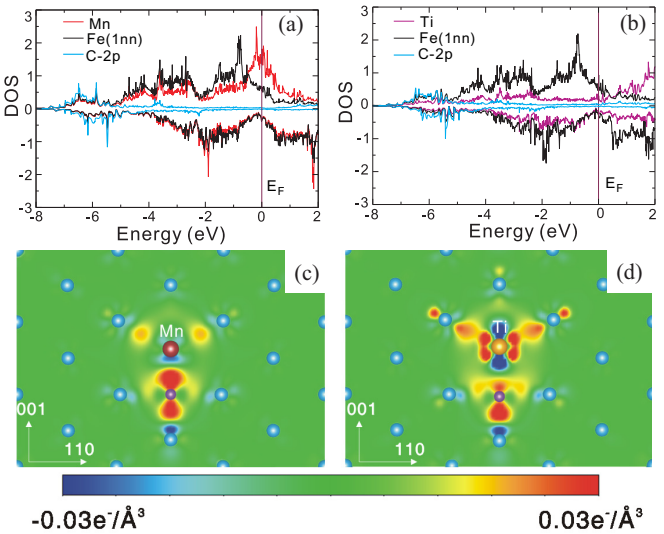

FIG. 4. (Color online) (a),(b) Local density of states calculated in the $Fe_{53}MC$ [M = Mn (a) and Ti (b)] supercell. (c),(d) Charge density difference map for a single C with (c) Mn and (d) Ti in the 1*nn* configuration. The blue balls and purple ball represent the Fe atoms and the C atom, respectively. The Mn and Ti atoms are both labeled.

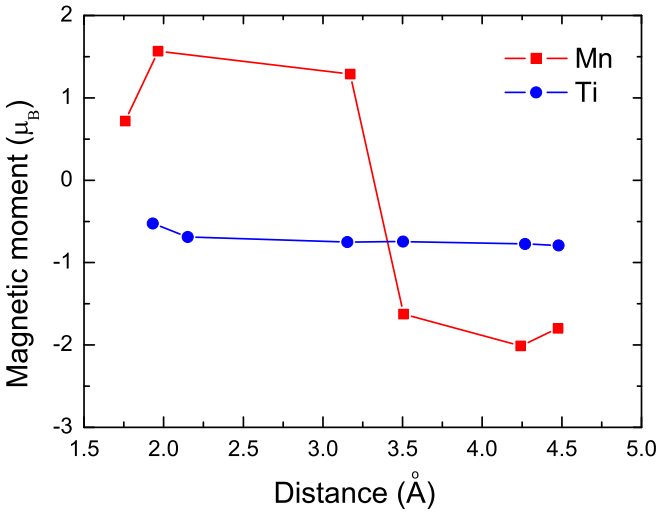

FIG. 5. (Color online) The local magnetic moment of the solute M (M = Mn and Ti) versus the M-C distance in the most energetically stable $Fe_{53}MC$ supercell.

Fe_{53}MnC supercell. This indicates that the Mn atom is so flexible in the magnetic moment that it can easily change its sign of the magnetic moment, which has been confirmed by the work of Bakaev's *et al.* [21]. However, the addition of carbon changes a little on the antiferromagnetic coupled magnetic moment of Ti. Besides, we further derived the magnetic moments of the solutes Mn and Ti as a function of the solute-C distance, as shown in Fig. 5. When the Mn-C distance is short, the ferromagnetic coupling between Mn and its nearby Fe atoms is more energetically favorable. However, as the Mn-C distance increases, Mn prefers the antiferromagnetic coupling with the neighboring Fe atoms. This fact reveals that carbon can stabilize the local ferromagnetic coupling between Mn and the neighboring Fe atoms, in agreement with the conclusion of Medvedeva *et al.* [43]. However, no obvious change is observed for the Ti-C case with the increasing Ti-C distance. It thus can be concluded that the magnetic couplings indeed play an important role for the abnormal Mn-C interactions.

In fact, there have been numerous efforts to elucidate the influence of the substitutional atoms on the Snoek peaks measured by the internal friction experiments [2,49–51]. Interestingly, it has been observed that the dilute addition (less than 1 mass%) of solutes M (Mn, P, Si, Al, Cr, and Co) in bcc Fe-C-M alloys reduces the normal Snoek peak height, but does not result in the appearance of any abnormal peaks [2]. Although the experimental conditions were far different from our current DFT considerations, within a qualitative level these experimental facts are still in agreement with our above analysis of the solute-C binding energies. Specifically, from our current calculations, almost all of M solutes exhibit large repulsive interactions with carbon in their 1nn and 2nn shells. This fact naturally reveals that the normal regions, where carbon would reside, should be reduced due to the M addition, leading to the reduction of the normal Snoek peak height. In contrast, it also needs to be noted that the attractive interactions between M and C are so weak that they cannot dramatically increase the number of C atoms in the influenced regions of the solutes. This fact interprets well the reason why no abnormal peak appears.

B. Solute M-vacancy-C interactions

As mentioned above, the microsegregation of carbon easily occurs in the bcc-type steels with the high Mn content [4,5]. Our above calculations for the Mn-C binding interactions seem consistent with these experimental observations. However, the attractive interaction between Mn and C at the 1nn configuration is only −0.08 eV, which is rather weak. Thus, it is hard to believe that the attractive 1nn Mn-C interaction is the main reason for the occurrence of carbon microsegregation in high-Mn steels [4,5].

Since the vacancy could be easily formed in the bulk, dislocation core, interfaces, and grain boundaries of the steels, we have attempted to introduce an Fe vacancy to form the so-called solute-vacancy-C complex. Interestingly, according to several previous studies [17,21,41], it has been noted that the Fe vacancy can serve as a strong carbon trapping site due to the large binding energy between the vacancy and C (−0.59 eV) [17] and the Fe vacancy also shows an attractive ability to bind the Mn atom with the largest binding energy at the 1nn configuration [21,41]. Even at the 3nn configuration, the Mn-vacancy interaction is still attractive [21,41]. The systematical calculations further revealed that the vacancy always exhibits the largest binding energy at the 1nn site with other M solutes in bcc Fe [21,41]. Therefore, it can be inferred that the M solutes and the vacancy can easily form the solute-vacancy pair in α-Fe. Here, based on those most stable configuration of the solute M-vacancy pair, we have further incorporated a single carbon atom into the M-vacancy pair. As shown in Fig. 6, there are six possible configurations by taking into account the symmetry. Our calculations demonstrated that the 5th configuration (called cgf^5), as illustrated in the inset of Fig. 7(a), was the most favorable in energy among the six configurations for all the 3d elements. Because of the tremendous computing workload, we did not do the test for the 4d and 5d rows elements. However, one can still reasonably trust that the cgf^5 one is also the most stable one for the 4d and 5d rows elements because in this configuration both the solute M and carbon are most strongly bound to the

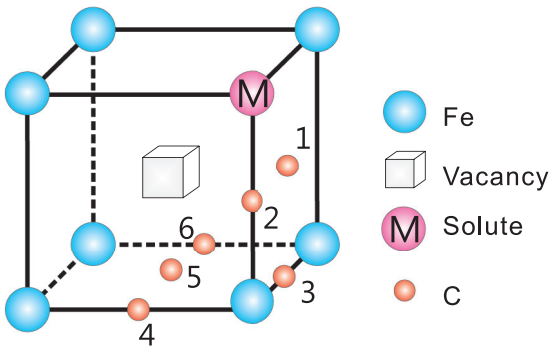

FIG. 6. (Color online) Solute M-vacancy-carbon configurations. The value i represents the position of the carbon in the ith configuration.

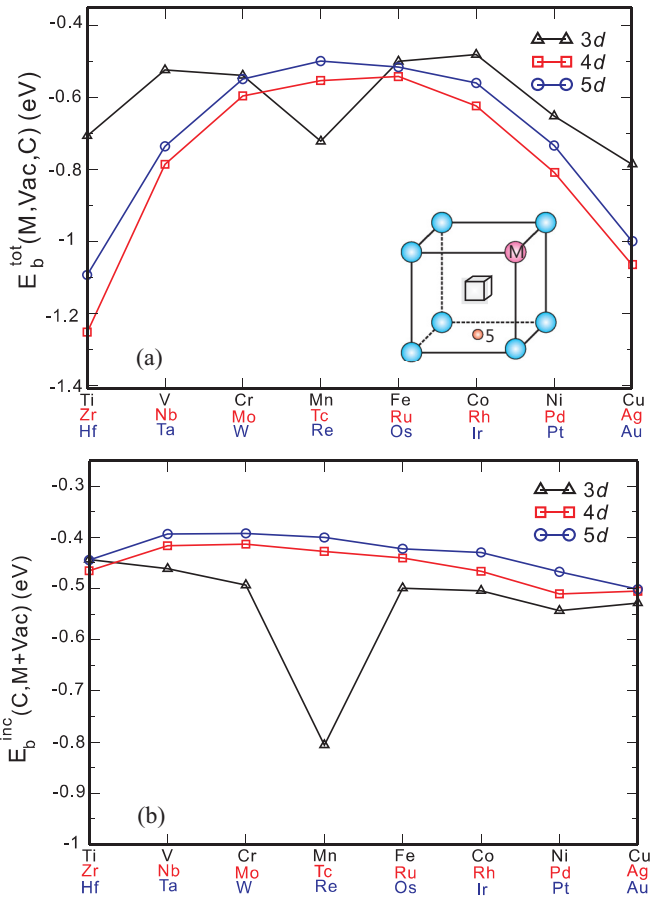

FIG. 7. (Color online) (a) The total binding energies among the solute M, carbon, and vacancy. (b) The incremental binding energies between the M-vacancy pair and carbon. $M = 3d$ (triangles), $4d$ (squares), and $5d$ (circles).

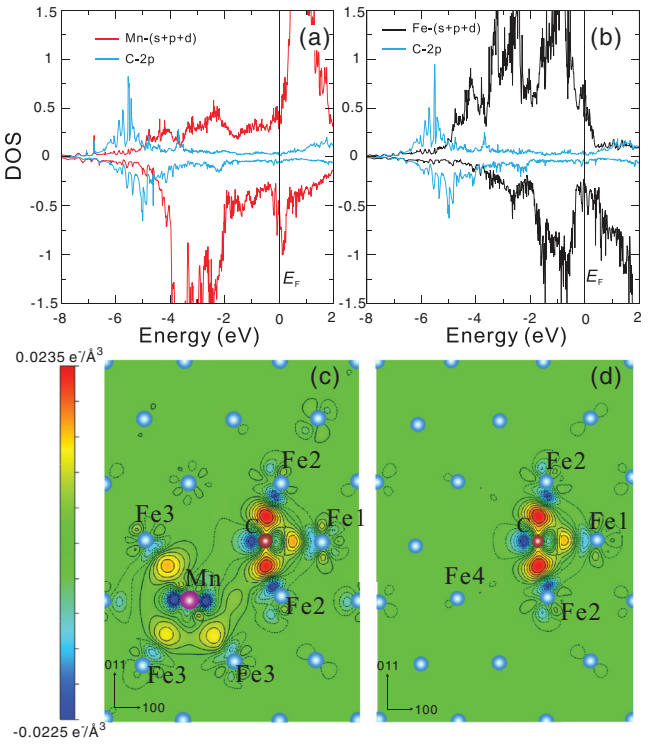

FIG. 8. (Color online) Local density of states of the Mn-C interaction (a) and of the Fe4-C interaction with Fe substituting Mn site (b) in the cfg^5 model and their corresponding charge density difference maps: Mn-vacancy-C (c) and Fe-vacancy-C (d). The Mn, Fe, and C atoms are all labeled.

vacancy [17,21,41] and the solute M-carbon interaction is less repulsive.

Figure 7(a) shows the total M-vacancy-C binding energies. The negative values indicate that when an Fe vacancy is introduced, the solute-vacancy-C complex becomes more energetically stable with respect to the isolated defects. It can thus be inferred that the solute, vacancy, and carbon would easily form a defect cluster in α-Fe. However, when we consider the contribution of the solute M-vacancy pair to the total binding energy (i.e., the incremental binding energy between the solute M-vacancy pair and carbon), the results are very unexpected. As elucidated in Fig. 7(b), with respect to the single Fe vacancy all the solute M-vacancy pairs for the $4d$ and $5d$ rows elements exhibit weaker binding energies with carbon. Surprisingly, the Mn-vacancy pair shows a significantly large attractive binding energy with carbon (about -0.81 eV). This value is nearly twice larger than those of other M-vacancy pairs with carbon [Fig. 7(b)].

We further compare the local density of states of the Mn-vacancy-C with those of the Fe-vacancy-C case in bcc Fe in Figs. 8(a) and 8(b). It can be seen that there is no obvious electronic hybridization between Mn [or Fe4 which just substitutes the Mn site as marked in Fig. 8(d)] and C. This is consistent with their charge difference maps where no charge accumulations are observed between Mn (or Fe4) and carbon. In contrast, the interstitial carbon atom shows the obvious electronic hybridizations with its $1nn$ Fe1 and $2nn$ Fe2 atoms, as visualized by the charge accumulations in Figs. 8(c) and 8(d). These comparisons suggest that the anomalous large binding energy between the Mn-vacancy pair and C does not originate from the electronic hybridization between Mn and C. Actually, the presence of the Fe vacancy results in an enhanced spin exchange splitting for Mn. From Fig. 8(a), the minority spin-down states are mostly located in the energy range from -4 to -2 eV whereas the majority spin-up states shift above the Fermi level, thereby causing the antiferromagnetic coupling with its $1nn$ Fe3 atom with a large magnetic moment of about $2.67\mu_B$ (see Table I). These strong magnetic couplings between Mn and Fe3, as illustrated by the accumulated charges in Fig. 8(c), play a crucial role in contributing to the anomalous large binding energy between the Mn-vacancy pair and C.

Furthermore, the influences of the Mn-vacancy pair on the carbon migration have also been analyzed, as compared with a single Fe vacancy. In order to eliminate the influence of the mirror images, the migration energy barriers were calculated using a larger supercell ($4 \times 4 \times 4$ bcc unit cell). As shown in Fig. 9, because of the large vacancy-C attraction on the $1nn$ shell and repulsion on the $2nn$ shell [52], the energy barrier of the carbon atom jumping back towards the vacancy is far lower than that of the carbon atom escaping away. Hence, we expect that carbon will return more frequently to the vacancy.

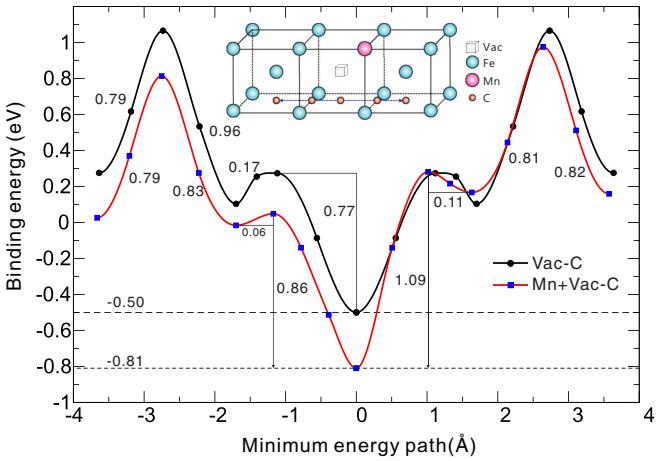

FIG. 9. (Color online) Carbon diffusion energy curves in the presence of a single vacancy or the Mn-vacancy pair in α-Fe. The embedded figure shows the corresponding migration pathways. The values near the curves represent the energy barrier.

A successful jump is found to occur when the C atom moves directly from one 1*nn o* site to another 1*nn o* site around the vacancy with the energy barrier of 0.83 eV, nearly the same as that for an isolated C atom jumping in the defect-free α-Fe. This fact suggests that the carbon motion is restricted within the cell centered around the vacancy position of the maximum bond with the C atom. When the Mn-vacancy pair is introduced, carbon will be trapped more significantly due to their stronger attractive interaction (−0.81 eV). Compared with a single Fe vacancy, on the one hand, the energy of Mn-vacancy-C system is much lower, indicating a more stable state. On the other hand, once the carbon is trapped by the Mn-vacancy pair, it will be more difficult for the carbon atom to escape from this deeper trap. Even though the carbon jumped to the second-nearest local minima by the thermal fluctuation, it could easily jump back to the original site because the energy barrier in the reverse direction is rather small (0.06–0.11 eV). This fact reveals that the vacancy assisted by Mn could indeed serve as a stronger trap to capture the carbon atoms.

Based on the above analysis, it is easily reminiscent of the occurrence of carbon microsegregation in high-Mn steels [4,5]. Although the interactions in practice are not the same as those in our case where the Mn and carbon are dilute, we can still draw some information from our current calculations for the first step to understand the nucleation of the carbon microsegregation around Mn. Specifically, Mn and vacancy can easily form a Mn-vacancy pair, not only in the bulk bcc Fe because of their attractive interactions [41], but also at the interfaces due to the attractive interactions [21] between Mn and the interfaces where there exists large free volume that might mimic the presence of the vacancies. Once Mn and vacancy form the pair, the carbon atoms would be strongly trapped by those Mn-vacancy pairs due to their large binding energies [see Fig. 7(b)]. In addition, this C-trap is so strong that carbon cannot easily escape from the vacancy because a large migration energy barrier is required (see Fig. 9). Both facts make the Mn-vacancy-C complex stable. Furthermore, it needs to be emphasized that here we only gave a tentative explanation on the nucleation of the microsegregation around Mn. In order to simulate the practical process, accurate and reasonable Fe-Mn-C potentials should be developed for larger scale simulations.

C. Influences of the dilute solutes on carbon's distribution and chemical potential

It is well accepted that substitutional solutes and carbon will redistribute in the solid solution during the heat treatment and thermal aging process. To investigate the effects of the solutes on the carbon's distribution, we further extend the solute-C interaction range to a farther one since the strain-induced *M*-C interactions are long range [7,53]. As illustrated in Table II, the solute *M* substitutes an Fe atom at the [000] position and the carbon atom varies at 12 positions up to the 12*nn* shell with respect to the solute *M*. It needs to be mentioned that there exist two inequivalent 5*nn* sites and no 11*nn* sites in our current supercell. Here we only take into account the solutes Si, Mn, Cr, and Al, because these elements are highly common in ferrite steels and numerous experimental studies [6,9,45,54,55] are available. As shown in Fig. 10, Cr displays repulsive interactions with C at all interacting distances, which is also the case for Mn, except for the 1*nn* configuration, where Mn presents a weak attractive interaction. However, Si and Al show the different behaviors. They display the repulsive interactions with C within a range of one lattice constant but weak attractive interactions beyond this distance. These computed solute-C interactions are quite consistent with the experimental observations concerning the influence of the alloying elements on the carbon solubility limit: Both Mn and Cr hardly change the carbon solubility limit, whereas Si increases it [3].

In general, within a short distance both the chemical interaction and strain-induced interaction contribute to the *M*-C binding energy. The chemical (or attractive) interaction is mostly due to the electronic structure effect. However, the chemical interaction's contribution is small here since only a few solutes show weak attractions with C. In contrast, the strain-induced interactions between the solutes and C are long range [7,53]. It is strong within short distances and decreases with the increasing distance. Therefore, it can be inferred that Mn has relatively large chemical interactions with C since it shows attractions with C in the 1*nn* site where the strain should be large. As the distance rises to a greater one, the chemical interactions become much weaker and hardly contribute to the *M*-C binding energy. Then the strain-induced interactions dominate. Thus, one can expect that the weak attractions

TABLE II. Relative positions of carbon at the different neighboring shells (*nn*) in the 3 × 3 × 3 bcc unit cell. The solute *M* substitutes Fe at the [000] site in all the configurations. The positions here are given in units of the α-Fe lattice constant (α_{bcc}).

Shell (*nn*)	1	2	3	4	5*a*	5*b*	6	7	8	9	10	12
C position	$[\frac{1}{2}00]$	$[\frac{1}{2}\frac{1}{2}0]$	$[1\frac{1}{2}0]$	$[1\frac{1}{2}\frac{1}{2}]$	$[11\frac{1}{2}]$	$[\frac{3}{2}00]$	$[\frac{3}{2}\frac{1}{2}0]$	$[\frac{3}{2}10]$	$[\frac{3}{2}1\frac{1}{2}]$	$[\frac{3}{2}11]$	$[\frac{3}{2}\frac{3}{2}0]$	$[\frac{3}{2}\frac{3}{2}1]$

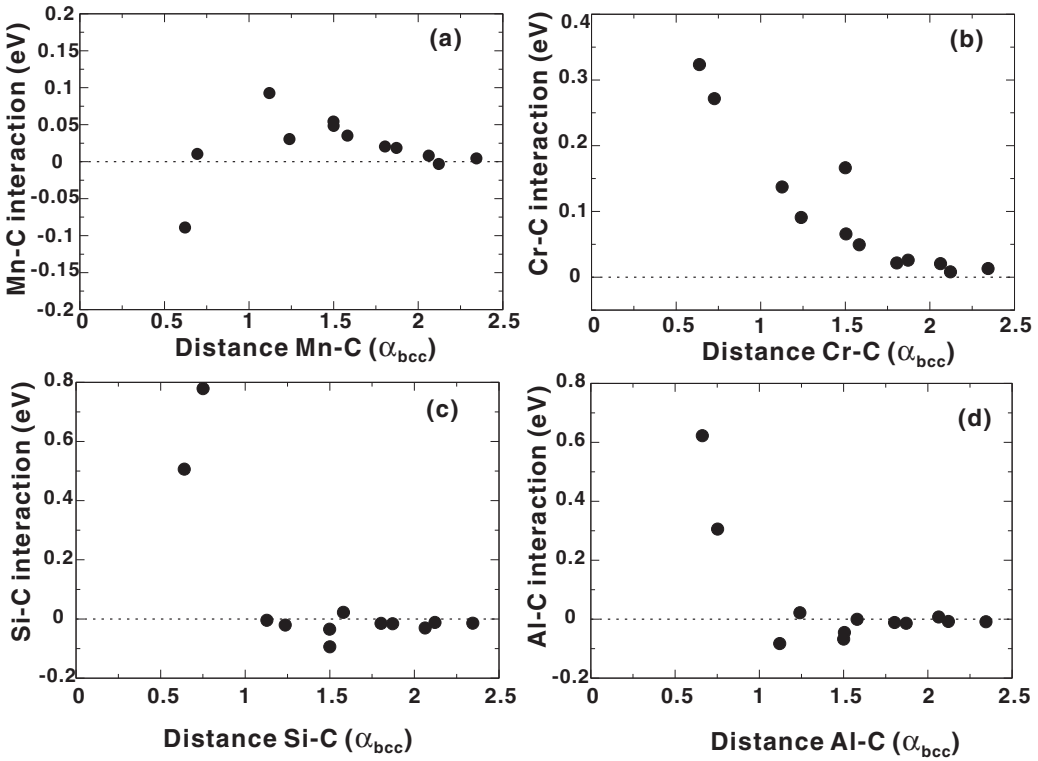

FIG. 10. Solute M-C binding energy versus the M-C distance in units of the bcc lattice constant. M = Mn (a), Cr (b), Si (c), and Al (d).

between Si (or Al) and C beyond the distance of one lattice constant are mainly caused by the strain relief. As the distance further increases beyond the cutoff radius, the M-C binding energy approaches zero.

Based on the thermodynamic considerations, Simonovic *et al.* [20] proposed a model to analyze how Si affects the interstitial carbon's distribution and chemical potential in α-Fe. Utilizing the obtained solute-C binding energies, we further extend the application of this model to other three elements (Cr, Mn, and Al). Figure 11 shows the carbon probability distribution in various neighbor shells around the solute atoms, and our results reproduce well the results of the carbon interacting with Si [20] [Fig. 11(a)]. One can see that there exist significant differences in the carbon distribution for different solutes. For instance, the carbon atoms can hardly be found in the 1nn and 2nn shells around Si atom due to their low fractions which are caused by the large repulsive interactions. Nevertheless, they would prefer to occupy the interstices between the 3nn and 6nn shells due to the weak attractions there. Al acts in a similar fashion. Strikingly, Mn is a unique element that displays the high carbon fraction in the 1nn site. As for Cr, within all the shells considered the carbon fractions are lower than that far beyond Cr.

Figure 12 shows the carbon fraction f_∞ in the octahedral interstitial sites beyond the solute-C interaction distance as a function of temperature for a given composition of $Fe_{0.99}M_{0.01}C_{0.001}$. According to Eq. (6), without the solute addition the f_∞ of the carbon in the Fe matrix for this composition should be a constant, giving $f_\infty = C_C/3 = 3.33 \times 10^{-4}$. It can be seen that the carbon fraction f_∞ for Mn, Si, and Al in the solid solution increase with the increasing temperature, which is different for Cr. At all temperatures considered, the carbon fraction f_∞ for the Si and Al addition are lower than that of Fe, whereas it is larger for the Cr addition. Only when the temperature is above 400 K will the carbon fraction f_∞ for the Mn addition exceed that in the pure Fe. Based on the theory of ideal solutions and in the dilute concentration limit, the chemical potential of the carbon can be approximated as Eq. (7). Accordingly, the carbons chemical potential is positively correlated with the carbon fraction far away from the solute. From Fig. 12 one can see that Si and Al additions would decrease the f_∞, whereas Cr and Mn increase it, compared with the original one in the matrix without any solute addition. As a result, it can be inferred that Si and Al have the potential ability to reduce the carbon's chemical potential, whereas Mn and Cr increase it.

D. Influences of the solutes on the carbon diffusion

The most likely and intuitive jumping mechanism for the interstitial diffusion of the carbon in the α-Fe lattice is the jump from an octahedral site (o site) to another nearest-neighboring one via the tetragonal site (t site) [14]. We have calculated the carbon diffusion migration energy barrier of 0.89 eV in the pure α-Fe, in good agreement with other DFT results of 0.86 eV [14] and 0.92 eV [16,56] and the experimentally measured data of 0.87 eV [57], 0.88 eV [58], and 0.84 eV [10]. Moreover, the diffusion prefactor D_0 has been further derived by DFT calculations according to the formula of $D_0 = \frac{1}{6}\alpha^2(\prod_{j=1}^{3N}\upsilon_j^{\rm ini}/\prod_{j=1}^{3N-1}\upsilon_j^{\rm sad})$ [14], where α is the lattice constant and $\upsilon_j^{\rm ini}$ and $\upsilon_j^{\rm sad}$ are the normal-mode frequencies at the initial and saddle-point state, respectively. Our result yields $D_0 = 1.56 \times 10^{-7}$ m^2/s. This value also agrees well with the previously calculated data of

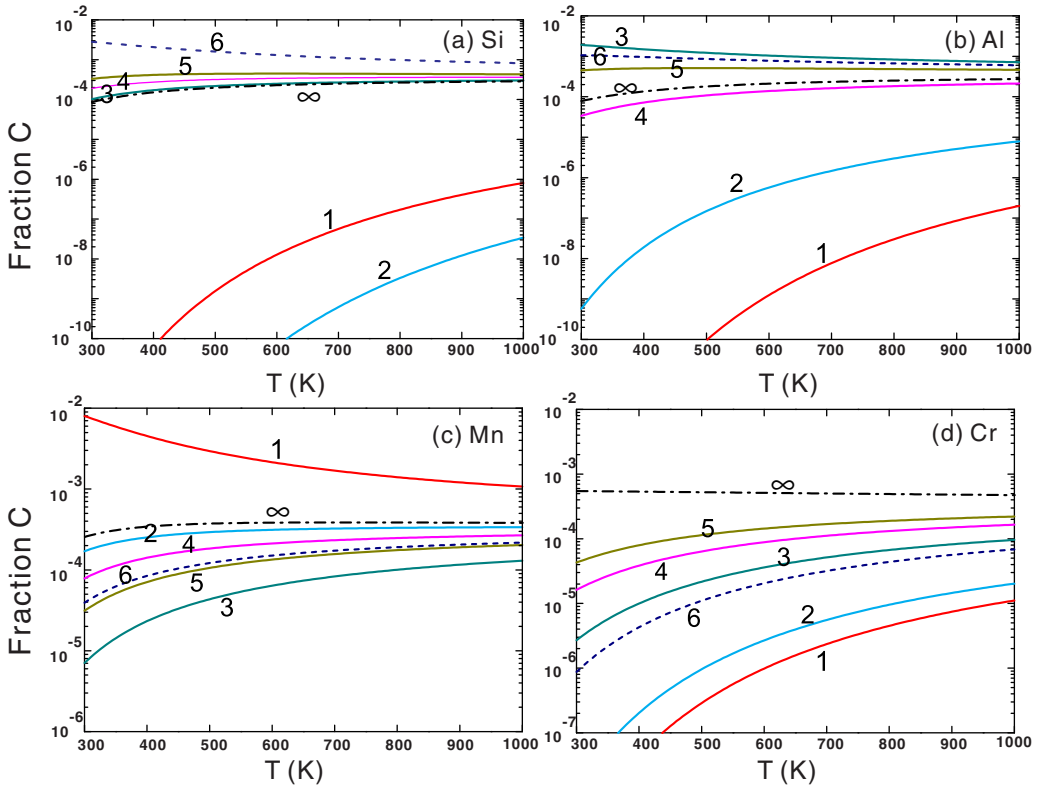

FIG. 11. (Color online) Carbon fraction at octahedral interstices for the first 6*nn* shells with respect to the solute atom M [M = Si (a), Al (b), Mn (c), and Cr (d)] and beyond (labeled with ∞) for a composition of $Fe_{0.99}M_{0.01}C_{0.001}$ (here $C_{0.001}$ denotes the fraction of carbon atoms occupying interstitial octahedral sites).

1.44×10^{-7} m^2/s [14] and 1.66×10^{-7} m^2/s [20], and the experimentally determined value of 1.67×10^{-7} m^2/s below 350 K [59]. In addition, we also used the kMC simulations to estimate D_0 for the C diffusion, obtaining a value of 2.14×10^{-7} m^2/s by fitting the computed C diffusivities to the temperatures according to Eq. (9), in nice agreement with above results.

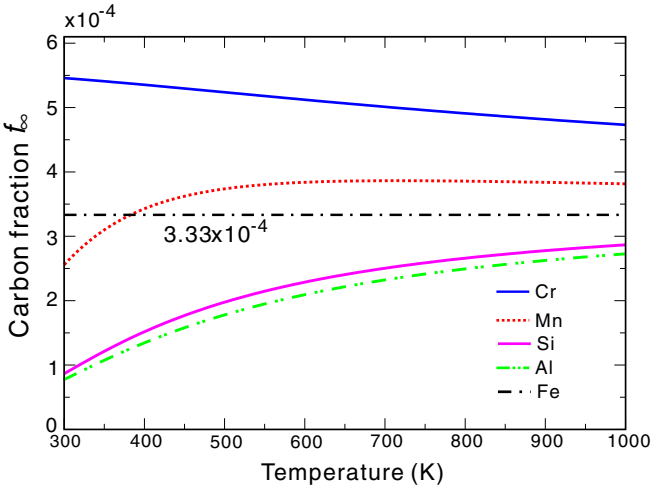

FIG. 12. (Color online) Carbon fraction f_∞ in the octahedral interstices beyond the solute M-C interaction distance as a function of temperature for a composition of $Fe_{0.99}M_{0.01}C_{0.001}$ (M = Mn, Cr, Si, and Al).

Next we focus on the effects of the dilute substitutional solutes M (M = Mn, Cr, Al, and Si) on the carbon's diffusion in α-Fe. We have considered all the possible diffusion pathways for the carbon jumping between two nearest-neighboring o sites in the presence of solute M using the CI-NEB method [32,33]. The calculated diffusion migration energy barriers ΔE were compiled in Table III. As an example, we further plotted the minimum-energy paths of the carbon migrating from the 1*nn* site to the 5*nn* site with respect to the solute Mn or Si in Fig. 13. Coupling these DFT energy barriers with the kMC simulations, the carbon diffusivity and effective migration energy barrier affected by the solute M have been computed at various solute concentrations and temperatures, as compiled in Table IV. The solute concentration-dependent trends were further presented in Fig. 14.

At first, it needs to be emphasized that we have reproduced well the results of the C diffusivity in the presence of Si obtained by Simonovic *et al.* [20]. Our data show the same order of magnitude and a similar tendency as theirs, but ours are much smaller, in particular at the low temperature. The discrepancy is likely due to the different migration energies used for the C diffusion. In our calculations, we considered the direction-dependent diffusion energy barriers. However, in Ref. [20] the kinetically resolved migration barrier (KRA approximation) proposed by Van der Ven *et al.* [60] has been employed. It was defined as the average of the forward and backward diffusion migration energies to overcome the difficulties associated with the direction dependence of the diffusion migration energy. It is really a good approximation

TABLE III. Diffusion migration energy barriers ΔE (eV) for the C atom jumping between two nearest-neighbor o sites relative to the solute M (M = Mn, Cr, Al, and Si). The positions for the solute M and carbon are shown in the Table II.

Initial → Final	Mn ΔE	Cr ΔE	Al ΔE	Si ΔE	Initial → Final	Mn ΔE	Cr ΔE	Al ΔE	Si ΔE
1 → 2	0.89	0.90	0.90	1.04	2 → 1	0.79	0.96	1.22	0.77
2 → 3	0.94	0.77	0.64	0.59	3 → 2	0.86	0.90	1.03	1.38
3 → 4	0.83	0.89	1.01	0.99	4 → 3	0.89	0.93	0.91	1.02
4 → 5	0.86	0.90	0.93	0.95	5 → 4	0.84	0.93	1.00	0.95
5 → 6	0.92	0.81	0.96	1.03	6 → 5	0.95	1.04	0.82	0.80
6 → 7	0.92	0.90	0.95	0.93	7 → 6	0.95	0.95	0.97	1.00
7 → 8	0.93	0.93	0.94	0.95	8 → 7	0.94	0.94	0.95	0.94
8 → 9	0.91	0.91	0.95	0.92	9 → 8	0.93	0.93	0.91	0.95
3 → 6	0.92	0.88	0.98	0.97	6 → 3	0.94	0.92	0.90	0.92
5 → 8	0.93	0.94	0.93	0.95	8 → 5	0.94	0.93	0.95	0.95
7 → 10	0.93	0.92	0.95	0.94	10 → 7	0.98	0.93	0.96	0.96
9 → 12	0.95	0.94	0.93	0.95	12 → 9	0.95	0.93	0.98	0.95

only when the thermodynamic energy difference before and after the C jump is much smaller than the corresponding kinetic parts [60]. This kinetic part was assumed to be equal to the migration energy for the C diffusion at the infinite distance away from the solute atom. However, from our calculations it was found that for the Si addition case the thermodynamic part has the same order of magnitude with the kinetic part within the 3nn shells, disobeying this KRA approximation [60]. Therefore, it would be more reasonable to fully take into account the direction-dependent diffusion energy barriers for each jump in computing the carbon diffusivity.

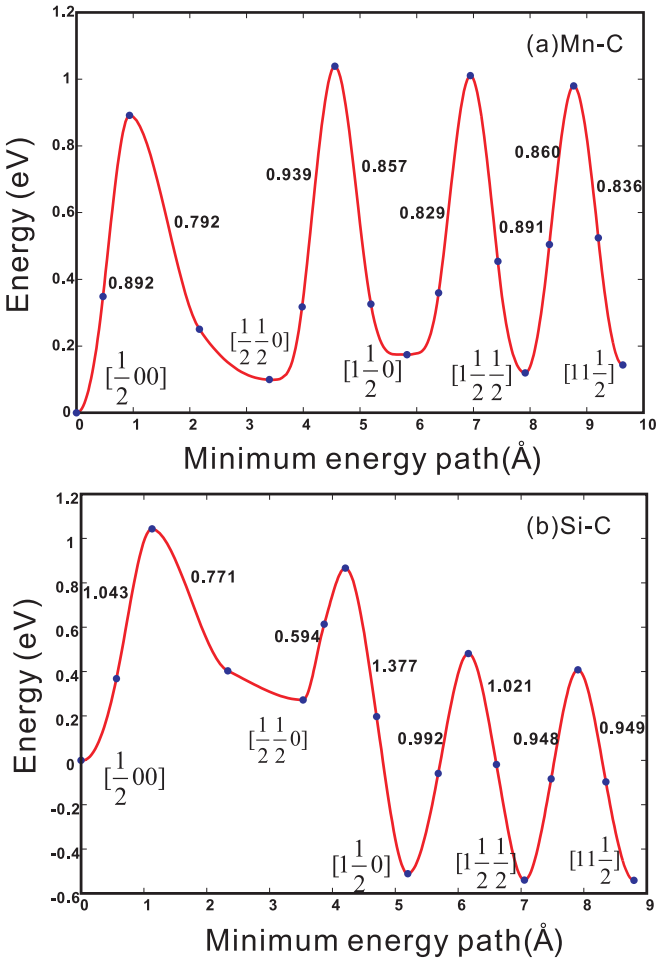

FIG. 13. (Color online) The minimum-energy paths of the carbon migrating from the 1nn to the 5nn o sites with respect to the solute Mn (a) or Si (b) in α-Fe. The values with and without square brackets represent the carbon's positions (see Table II) and the energy barriers, respectively.

Furthermore, it can be found from Fig. 14 that, in the range of dilute solute concentration Mn exhibits little influence on the carbon diffusivity (because it does not significantly alter the carbon diffusion energy barriers), whereas Cr, Al, and Si all remarkably reduce the carbon diffusivity, particularly at low temperature (i.e., 500 K). Taking, Si for instance, the 0.78 at.% content of Si significantly reduces the C diffusivity with 73% at 500 K and 32% at 1000 K than those without the Si addition. This is due to the fact that Si greatly affects the migration energy barriers of the carbon diffusion, as shown in Fig. 13. Specifically, the 1nn and 2nn o sites around Si are so high in energy that it is more difficult for carbon to stay, thereby significantly reducing the positions where the carbon can diffuse. At the longer distance beyond the 3nn shells, the carbon atom is trapped by Si with a weak attraction, which increases the residence time of carbon to stay at these sites. Both of the above situations would contribute to the significant reduction of the carbon diffusion. A similar behavior is also observed for the Al addition. As for Cr, its reduction on the C diffusivity is less apparent since only a labyrinth mechanism [20] works due to its repulsive interactions with C in all the 12 nearest-neighboring shells.

Our simulated results also demonstrate that, with increasing the solute concentration of Cr (Al or Si), the C diffusivity decreases significantly (see Fig. 14). Interestingly, at low temperature the Si (or Al) addition makes carbon atoms most likely sit at the attractive-interaction region around the solute, remarkably decreasing carbon diffusivity (i.e., 500 K in Fig. 14). It indicates that the carbon diffusion is indeed dominated by the so-called trapping mechanism [61] at the low temperature. However, the high-temperature kMC simulations reveal that the carbon atom would randomly occupy any interstitial o sites. In this situation, both the labyrinth

TABLE IV. kMC simulated carbon diffusivity D (in m^2/s) and effective migration energy ΔE (in eV) in α-Fe as a function of the solute concentration C_M (in at.%) (M = Mn, Cr, Al, and Si) at temperatures of 500 K and 1000 K.

	Mn			Cr			Al			Si		
C_M (at.%)	500 K (10^{-16})	1000 K (10^{-12})	ΔE (eV)	500 K (10^{-16})	1000 K (10^{-12})	ΔE (eV)	500 K (10^{-16})	1000 K (10^{-12})	ΔE (eV)	500 K (10^{-16})	1000 K (10^{-12})	ΔE (eV)
0.00	2.55	7.38	0.89	2.55	7.38	0.89	2.55	7.38	0.89	2.55	7.38	0.89
0.15	2.59	7.30	0.88	2.43	7.15	0.89	2.27	7.00	0.89	1.83	6.90	0.91
0.40	2.58	7.13	0.88	2.15	6.75	0.89	1.81	6.35	0.90	1.09	6.08	0.94
0.78	2.61	6.83	0.88	1.76	6.03	0.90	1.29	5.35	0.92	0.68	5.03	0.94
1.39	2.68	6.83	0.86	1.33	5.35	0.91	0.87	4.25	0.93	0.49	3.83	0.97
1.85	2.83	7.10	0.87	1.04	4.88	0.93	0.54	3.45	0.95	0.37	3.15	0.98

mechanism [20] and the trapping mechanism [61] work well. As evidenced in our simulations, at high temperature (i.e., 1000 K in Fig. 14) the alloying addition results in a smaller impact on the carbon diffusivity.

The influences of the Al concentration on the carbon diffusion in Fe-Al-C alloys have also been investigated experimentally by Strahl and Golovin *et al.* [6]. They observed that with increasing the Al content the Snoek peak became broader and its corresponding position shifted upward the higher temperature. Similar phenomenon was also observed in the Fe-Cr-C alloys [62]. It is known that the Snoek peak is a typical relaxational internal friction peak due to the migration of the interstitial atoms induced by the stress. In the bcc Fe-C alloys without any solutes, where all the o sites are equivalent for the carbon, the individual migration energy barrier and effective migration energy barrier ΔE are the same for each jump of carbon. Thus, the relaxation time τ [$\tau = \tau_0 \exp(\Delta E/k_B T)$] should be nearly constant; i.e., the resonance condition is almost strictly satisfied, leading to the appearance of the narrow Snoek peak. However, when Al is added, it would greatly affect the potential energy surface and the distribution of the interstitial carbon atoms, which makes the resonance condition in the internal friction measurements less strict to meet. That is the reason why the Snoek peak broadens when Al is added. The center of the wide peak corresponds to the effective migration energy barrier of the carbon. Within our kMC simulations it was also found that with increasing the Al content, the effective migration energy barrier of the carbon diffusion increases (see Table IV). This fact indicates that a much higher temperature is required to activate the migration of the carbon, coinciding well with the experimentally observed upper shift of the Snoek peak to the higher temperature [6].

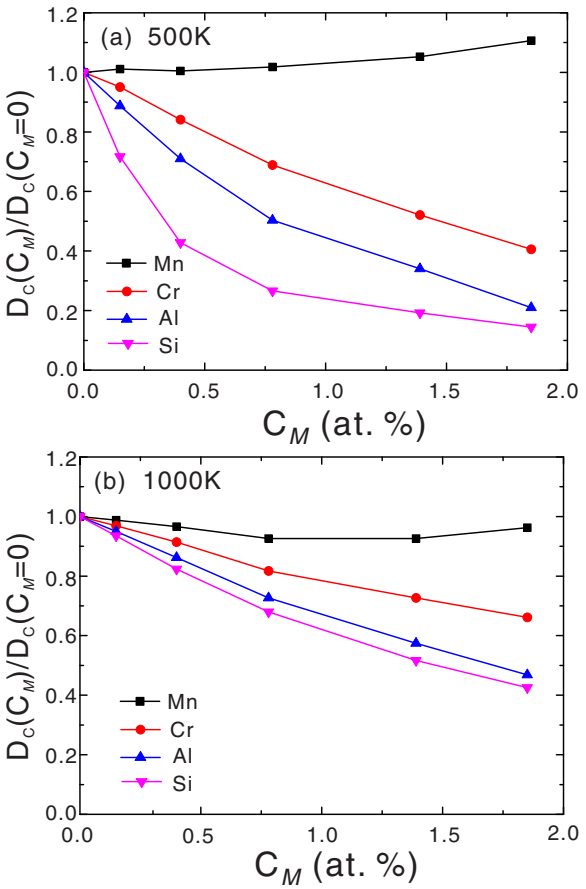

FIG. 14. (Color online) Carbon diffusivities in the presence of the solute M (M = Mn, Cr, Al, and Si) relative to that without M versus the solute concentrations at temperatures of 500 K and 1000 K.

IV. CONCLUSIONS

In the present paper, we have systematically investigated the dilute solute-C and solute-vacancy-C interactions and the influences of dilute solutes on the carbon's distribution and diffusion in α-Fe through first-principles calculations. The main conclusions are as follows.

(i) In terms of the 4d and 5d elements, the solute-C interactions are mostly governed by the strain relief, whereas for the 3d elements, magnetic coupling and electronic structure also play important roles, which may override the strain relief. Mn is the only element that shows attractive interactions with C in the 1nn shell.

(ii) When an Fe vacancy is introduced, the solute-vacancy-carbon total binding energies become negative, indicating the easy formation of the defects complex. In particular, the Mn-vacancy pair exhibits an exceptionally large binding energy with C (−0.81 eV), which is due to the stronger antiferromagnetic coupling between Mn and its nearest-neighboring Fe atoms assisted by the Fe vacancy. Moreover, our results also suggest that the vacancy assisted by Mn could serve as a stronger trap site to the carbon.

(iii) The longer-range interactions between the dilute solutes (Mn, Cr, Al, and Si) and C have been investigated in detail. Through the model proposed by Simonovic *et al.* [20] coupled with the thermodynamic considerations, it has been found that the solutes' addition would greatly affect the carbon distribution and chemical potential. Among the four solutes, Mn and Cr tend to increase the carbon chemical potential, whereas Al and Si reduce it.

(iv) The carbon diffusion affected by the dilute solutes has been modeled in depth through the kMC simulations coupled with the DFT energy barrier calculations. The results demonstrate that in the range of the dilute concentration, Mn hardly changes the carbon diffusivity, whereas Cr, Al, and Si significantly decrease it as the concentration increases.

Finally, we would like to emphasize that our current first-principles calculations only fit to the cases where the alloying solutes and carbon are dilute in α-Fe. When compared with the available experimental results, one should be always cautious about complicated experimental factors, such as temperature, pressure, concentration, and defects, and so on.

ACKNOWLEDGMENTS

This work was supported by the "Hundred Talents Project" of the Chinese Academy of Sciences, the Major Research Plan (Grant No. 91226204) of the NSFC of China (Grants No. 51174188 and No. 51074151), and the Beijing Supercomputing Center of CAS (including its Shenyang branch).

[1] R. Abbaschian, L. Abbaschian, and R. E. Reed-Hill, *Physical Metallurgy Principles* (Cengage Learning, Stamford, 2009).
[2] H. Saitoh, N. Yoshinaga, and K. Ushioda, Acta Mater. **52**, 1255 (2004).
[3] H. Saitoh, K. Ushioda, N. Yoshinaga, and W. Yamada, Scr. Mater. **65**, 887 (2011).
[4] K. Suzuki and T. Miyamoto, Trans. Iron Steel Inst. Jpn. **18**, 80 (1978).
[5] R. F. Zhu, Y. P. Lü, and T. Wei, Sci. China, Ser. E **40**, 567 (1997).
[6] A. Strahl, I. S. Golovin, H. Neuhäuser, S. B. Golovina, and H. R. Sinning, Mater. Sci. Eng. A **442**, 128 (2006).
[7] M. S. Blanter and L. B. Magalas, Scr. Mater. **43**, 435 (2000).
[8] I. S. Golovin, S. V. Divinski, J. Čížek, I. Procházka, and F. Stein, Acta Mater. **53**, 2581 (2005).
[9] D. Ruiz, J. L. Rivera-Tovar, D. Segers, R. E. Vandenberghe, and Y. Houbaert, Mater. Sci. Eng. A **442**, 462 (2006).
[10] F. Walz, T. Wakisaka, and H. Kronmüller, Phys. Status Solidi A **202**, 2667 (2005).
[11] S. Garruchet and M. Perez, Comput. Mater. Sci. **43**, 286 (2008).
[12] C. K. Ande and M. H. F. Sluiter, Metall. Mater. Trans. A **43**, 4436 (2012).
[13] A. G. Khachaturyan, *Theory of Structural Transformations in Solids* (Wiley, New York, 1983).
[14] D. E. Jiang and E. A. Carter, Phys. Rev. B **67**, 214103 (2003).
[15] D. E. Jiang and E. A. Carter, Phys. Rev. B **71**, 045402 (2005).
[16] C. Domain, C. S. Becquart, and J. Foct, Phys. Rev. B **69**, 144112 (2004).
[17] T. Ohnuma, N. Soneda, and M. Iwasawa, Acta Mater. **57**, 5947 (2009).
[18] Y. You, M. F. Yan, and H. T. Chen, Comput. Mater. Sci. **67**, 222 (2013).
[19] C. S. Becquart, J. M. Raulot, G. Bencteux, C. Domain, M. Perez, S. Garruchet, and H. Nguyen, Comput. Mater. Sci. **40**, 119 (2007).
[20] D. Simonovic, C. K. Ande, A. I. Duff, F. Syahputra, and M. H. F. Sluiter, Phys. Rev. B **81**, 054116 (2010).
[21] A. Bakaev, D. Terentyev, G. Bonny, T. P. C. Klaver, P. Olsson, and D. Van Neck, J. Nucl. Mater. **444**, 237 (2014).
[22] P. Hohenberg, Phys. Rev. **136**, B864 (1964).
[23] W. Kohn and L. J. Sham, Phys. Rev. **140**, A1133 (1965).
[24] G. Kresse and J. Hafner, Phys. Rev. B **47**, 558 (1993).
[25] G. Kresse and J. Furthmüller, Phys. Rev. B **54**, 11169 (1996).
[26] P. E. Blöchl, Phys. Rev. B **50**, 17953 (1994).
[27] J. P. Perdew, K. Burke, and M. Ernzerhof, Phys. Rev. Lett. **77**, 3865 (1996).
[28] D. J. Singh, W. E. Pickett, and H. Krakauer, Phys. Rev. B **43**, 11628 (1991).
[29] T. Klymko and M. H. F. Sluiter, J. Mater. Sci. **47**, 7601 (2012).
[30] W. A. Counts, C. Wolverton, and R. Gibala, Acta Mater. **58**, 4730 (2010).
[31] C. Kittel, *Introduction to Solid State Physics* (Wiley, New York, 1996).
[32] G. Henkelman, B. P. Uberuaga, and H. Jonsson, J. Chem. Phys. **113**, 9901 (2000).
[33] D. Sheppard, R. Terrell, and G. Henkelman, J. Chem. Phys. **128**, 134106 (2008).
[34] M. H. Kalos and P. A. Whitlock, *Monte Carlo Methods: Basics* (Wiley, New York, 1986), Vol. 1.
[35] W. Pascheto and G. P. Johari, Metall. Mater. Trans. A **27**, 2461 (1996).
[36] M. Lübbehusen and H. Mehrer, Acta Metall. Mater. **38**, 283 (1990).
[37] S. Huang, D. L. Worthington, M. Asta, V. Ozolins, G. Ghosh, and P. K. Liaw, Acta Mater. **58**, 1982 (2010).
[38] J. C. Christopher, *Essential of Computational Chemistry: Theories and Models* (Wiley, UK, 2002).
[39] A. B. Bortz, M. H. Kalos, and J. L. Lebowitz, J. Comput. Phys. **17**, 10 (1975).
[40] H. Mehrer, *Diffusion in Solids: Fundamentals, Methods, Materials, Diffusion-Controlled Processes* (Springer, Germany, 2007).
[41] P. Olsson, T. P. C. Klaver, and C. Domain, Phys. Rev. B **81**, 054102 (2010).
[42] N. Sandberg, K. O. E. Henriksson, and J. Wallenius, Phys. Rev. B **78**, 094110 (2008).
[43] N. I. Medvedeva, D. C. Van Aken, and J. E. Medvedeva, J. Phys.: Condens. Matter **23**, 326003 (2011).
[44] H. Numakura, G. Yotsuit, and M. Koiwa, Acta Metall. Mater. **43**, 705 (1995).

[45] V. Massardier, E. L. Patezour, M. Soler, and J. Merlin, Metall. Mater. Trans. A **36**, 1745 (2005).
[46] H. Abe, T. Suzuki, and S. Okada, Trans. Jpn. Inst. Met. **25**, 215 (1984).
[47] H. Abe, J. Korean Inst. Met. **24**, 612 (1986).
[48] T. Nishizawa, Bull. Jpn. Inst. Met. **12**, 401 (1973).
[49] C. Wert, J. Metals **4**, 602 (1952).
[50] H. Numakura and M. Koiwa, *International Symposium on M3D III: Mechanics and Mechanisms of Material Damping*, edited by A. Wolfenden and V. K. Kinra (ASTM, West Conshohocken, PA, 1997), pp. 383–393.
[51] H. Numakura and M. Koiwa, J. Phys. IV France **06**, C8-97 (1996).
[52] K. Tapasa, A. Barashev, D. Bacon, and Y. Osetsky, Acta Mater. **55**, 1 (2007).
[53] M. S. Blanter, J. Alloys Compd. **291**, 167 (1999).
[54] I. S. Golovin IS, H. Neuhäuser, A. Rivière, and A. Strahl, Intermetallics **12**, 125 (2004).
[55] I. S. Golovin and S. B. Golovina, Phys. Met. Metallogr. **102**, 593 (2006).
[56] C. Domain, J. Nucl. Mater. **351**, 1 (2006).
[57] C. A. Wert, Phys. Rev. **79**, 601 (1950).
[58] S. Takaki, J. Fuss, H. Kugler, U. Dedek, and H. Schults, Radiat. Eff. **79**, 87 (1983).
[59] J. R. G. da Silva and R. B. McLellan, Mater. Sci. Eng. **26**, 83 (1976).
[60] A. Van der Ven, G. Ceder, M. Asta, and P. D. Tepesch, Phys. Rev. B **64**, 184307 (2001).
[61] C. A. Wert and R. C. Frank, Annu. Rev. Mater. Sci. **13**, 139 (1983).
[62] I. S. Golovin, M. S. Blanter, and R. Schaller, Phys. Stat. Sol. A **160**, 49 (1997).